HHS Public Access

Author manuscript

Magn Reson Med. Author manuscript; available in PMC 2019 July 01.

Published in final edited form as:

Magn Reson Med. 2018 July ; 80(1): 286–293. doi:10.1002/mrm.27030.

Optimization and Validation of Accelerated Golden-angle Radial Sparse MRI Reconstruction with Self-Calibrating GRAPPA Operator Gridding

Thomas Benkert[1], **Ye Tian**[2,3], **Chenchan Huang**[1], **Edward V. R. DiBella**[2], **Hersh Chandarana**[1], and **Li Feng**[1]

[1]Center for Advanced Imaging Innovation and Research (CAIR), and Bernard and Irene Schwartz Center for Biomedical Imaging, Department of Radiology, New York University School of Medicine, New York, NY, United States

[2]Department of Radiology and Imaging Sciences, University of Utah, Salt Lake City, Utah, United States

[3]Department of Physics and Astronomy, University of Utah, Salt Lake City, Utah, United States

Abstract

Purpose—Golden-angle RAdial Sparse Parallel (GRASP) MRI reconstruction requires gridding and re-gridding to transform data between radial and Cartesian k-space. These operations are repeatedly performed in each iteration, which makes the reconstruction computationally demanding. This work aimed to accelerate GRASP reconstruction using self-calibrating GRAPPA operator gridding (GROG) and to validate its performance in clinical imaging.

Methods—GROG is an alternative gridding approach based on parallel imaging, where k-space data acquired on a non-Cartesian grid are shifted onto a Cartesian k-space grid using information from multi-coil arrays. For iterative non-Cartesian image reconstruction, GROG is performed only once as a pre-processing step. Therefore, the subsequent iterative reconstruction can be performed directly in Cartesian space, which significantly reduces computational burden. Here, a framework combining GROG with GRASP (GROG-GRASP) is first optimized and then compared with standard GRASP reconstruction in twenty-two prostate patients.

Results—GROG-GRASP achieved ~4.2-fold reduction in reconstruction time compared to GRASP (~333 minutes v.s. ~78 minutes) while maintaining image quality (SSIM≈0.97 and RMSE≈0.007). Visual image quality assessment by two experienced radiologists did not show significant differences between the two reconstruction schemes. With a GPU implementation, image reconstruction time can be further reduced to ~14 minutes.

Conclusion—GRASP reconstruction can be substantially accelerated using GROG. This framework is promising towards broader clinical application of GRASP and other iterative non-Cartesian reconstruction methods.

Address correspondence to: Li Feng, PhD, Center for Advanced Imaging Innovation and Research (CAI^{2}R), Department of Radiology, New York University School of Medicine, 660 First Ave, New York, NY 10016, Phone: 212-263-0409, Fax: 212-263-7541, Li.Feng@nyumc.org.

Keywords

GRASP; GROG; Gridding; non-Cartesian; iterative reconstruction

Introduction

Interest in the use of radial sampling for clinical MRI has been rapidly increasing during the past few years. It has been applied for many clinical studies (1) including cardiac (2–7), abdominal (8–12), breast (13–15), and neuro (16–18) imaging. Radial trajectories exhibit inherently incoherent undersampling behavior, which makes this sampling strategy an attractive acquisition scheme for the application of sparsity-based reconstruction methods (19–22). Compared to conventional Cartesian sampling, radial sampling has lower sensitivity to motion (23) and enables continuous data acquisitions when a golden-angle reordering scheme is used (24). These features are attractive for many dynamic post-contrast imaging applications.

Golden-angle RAdial Sparse Parallel (GRASP) MRI (21) is a framework that combines multi-coil compressed sensing reconstruction with golden-angle radial sampling and has been successfully applied for different clinical applications (25). However, one of the major barriers that limits broader applicability of GRASP as well as many other iterative non-Cartesian reconstruction methods in clinical routine is the long reconstruction time. This is mainly attributed to **a)** the iterative nature of compressed sensing and **b)** an additionally required step to interpolate the k-space from a non-Cartesian grid onto a Cartesian grid prior to the fast Fourier transform (FFT). Such an interpolation process is known as gridding and is usually implemented via convolution of the non-Cartesian k-space with a predefined kernel. This gridding step, together with a re-gridding step that transforms data back to non-Cartesian k-space, are repeatedly performed for each iteration in GRASP. This adds increasing burden to the reconstruction that is already computationally expensive.

Several methods can enable iterative non-Cartesian reconstruction without performing gridding/regridding during iterations, thus reducing image reconstruction burden. For example, non-Cartesian data can be simply interpolated onto a Cartesian grid in a pre-processing step prior to the iterative process (20). Alternatively, the Toeplitz-structure of the forward and backward encoding operators (i.e., $E^H E$) can be exploited, which allows replacing the gridding steps by a simple multiplication with the FFT of the pre-calculated point-spread function of the sampling process (26–28). GeneRalized autocalibrating partially parallel acquisitions Operator Gridding (GROG) (29) is another promising technique to speed up iterative non-Cartesian image reconstruction. GROG shifts non-Cartesian k-space data onto a Cartesian grid using parallel imaging in a one-to-one mapping process. Therefore, the synthesized k-space can be treated as a dataset of Cartesian samples, enabling reduction of reconstruction time by performing the subsequent iterative process directly in Cartesian space.

The feasibility of combining GROG with iterative non-Cartesian image reconstruction has been investigated in several studies. For example, it has been applied to non-Cartesian MR parameter mapping (30), real-time mouse imaging (31), dynamic-contrast-enhanced (DCE)

MRI (32,33), and cardiac perfusion imaging (34). These results showed that GROG enables remarkable reduction of reconstruction time without sacrificing image quality or temporal fidelity. However, the approach has never been systematically evaluated in a clinical setting. In this work, we aimed to **i)** extend the GRASP approach by incorporating GROG, **ii)** further optimize this framework for improved reconstruction performance, and **iii)** evaluate the performance of this approach in clinical patient scans.

Methods

GROG-GRASP: Extending GRASP with Self-Calibrating GROG

Density Compensation Filter in GROG—Conventional non-Cartesian image reconstruction begins with a step for sampling density compensation, followed by convolution gridding, inverse FFT (iFFT), and deapodization to generate the final image. In radial imaging, a Ram-Lak filter, which is referred to as rDCF hereafter, is often used for density compensation. In contrast, a GROG reconstruction first shifts all radial k-space points onto a Cartesian grid, resulting in a Cartesian k-space where data are distributed in a pseudo-radial pattern (see Figure S1 in supplementary materials). The GROG process is performed as

$$S(k_x+\delta_x, k_y+\delta_y) = G_x^{\delta x} G_y^{\delta y} S(k_x, k_y) \quad [1]$$

where each radial k-space point at location $[k_x,k_y]$ is shifted to its nearest Cartesian position at $[k_x+\delta_x,k_y+\delta_y]$ by a distance of δ_x and δ_y in k_x and k_y direction, respectively. G_x *and* G_y represent weights used for the shifting, which can be pre-calculated using acquired radial k-space data (35). Before applying the iFFT, the sampling density is compensated by dividing the estimated Cartesian k-space by the *GROG Density*, which is a matrix indicating the number of samples that fall onto each Cartesian position. If no point is shifted to a given Cartesian position, the *GROG Density* is set to one at this position. The GROG density compensation filter (gDCF) for n spokes can then be defined as:

$$gDCF\left(k_x, k_y\right)_n = \frac{1}{GROG\ Density\left(k_x, k_y\right)_n} \quad [2]$$

Figure 1 compares the undersampling behavior between convolution gridding and GROG using a radial prostate dataset with 26 spokes and an in-plane matrix size of 224×224. Figure 1a shows the image reconstructed using convolution gridding with rDCF (Ram-Lak filter), which was implemented using the non-uniform FFT (NUFFT) toolbox (36). Figure 1b shows the image reconstructed using GROG with $gDCF_{default}$, where $gDCF_{default}$ indicates the gDCF calculated using the same number of spokes used for image reconstruction (i.e., $gDCF_{n=26}$ in this case). While NUFFT generated a sharp image, GROG introduced noticeable blurring with $gDCF_{default}$. This can be attributed to the fact that $gDCF_{default}$ prefers signal to noise ratio (SNR) over resolution as described in (26,34). Figure 1c shows images reconstructed using GROG, where gDCF was calculated with a larger number of

spokes than that used for image reconstruction (n>26). With increasing n, the visual sharpness of the reconstructed images is improved, indicating that the use of gDCF with a large n can resolve blurring in GROG reconstruction.

From GRASP to GROG-GRASP—In the standard GRASP reconstruction (Figure 2a), the optimization starts with the dynamic multi-coil radial k-space after data sorting (21). During each iteration, the radial k-space data are first interpolated onto a Cartesian grid with a convolution, followed by an iFFT to generate an image-series. After optimization update, the image is transformed back to radial k-space to enforce data consistency. Such iteration is repeatedly performed until a certain stopping criterion is reached. The cost function is formulated as:

$$d = \underset{d}{\operatorname{argmin}} \frac{1}{2}\left\|Ed - \sqrt{D}S\right\|_2^2 + \lambda\left\|Td\right\|_1 \quad [3a]$$

$$E = \sqrt{D}GFC \quad [3b]$$

Here, F is the FFT operator, C represents coil sensitivity maps, d is the to-be-reconstructed dynamic image series, S is the sorted radial k-space data, G represents the convolution gridding operator, and T is a sparsifying transform. The rDCF (D in Equation 3) is included in the iterative process to speed up convergence (37). To ensure that the encoding operator E and its Hermitian transpose (denoted as E^H) are adjoint, rDCF is separated into two square root terms, one applied in a pre-compensation step before each iteration and the other one applied during each iteration as shown in Figure 2a.

In the modified GRASP framework using GROG (referred to as GROG-GRASP), GROG is performed as a pre-processing step to generate corresponding dynamic multi-coil Cartesian k-space data (Figure 2b). The iterative reconstruction is then performed by solving:

$$d = \underset{d}{\operatorname{argmin}} \frac{1}{2}\left\|Ed - \sqrt{W}S_c\right\|_2^2 + \lambda\left\|Td\right\|_1 \quad [4a]$$

$$E = \sqrt{W}FC \quad [4b]$$

Here, S_c represents Cartesian k-space data after GROG. Therefore, mapping during the iterative process is only performed between image space and Cartesian k-space. As shown in Figure 2b, $\mathrm{gDCF}_{\mathrm{default}}$ is applied in the GROG process to compensate for the radial sampling density. To ensure fast convergence, an additional filter, referred to as GROG weighting filter (W), is calculated using the following equation:

$$W = \frac{gDCF_n}{gDCF_{default}} \quad [5]$$

This filter is incorporated in each iteration, with a role similar to the rDCF in standard GRASP. The design of W is based on the observation from Figure 1 that gDCF for a large n resolves the blurring effect caused by the variable-density pseudo radial data distribution. When n equals the number of spokes used for reconstructing each frame, $gDCF_n$ equals $gDCF_{default}$ and therefore, no additional weighting (W=1) is applied. As in the standard GRASP reconstruction, W is separated into two square root terms to ensure that E and E^H in Equation 4 are adjoint.

The computational complexity of single-threaded 2D convolution gridding and subsequent FFT can be calculated as (38):

$$\underbrace{c_1 \cdot M \cdot K_1, K_2}_{Convolution} + \underbrace{c_2 \cdot N \cdot \log(N)}_{FFT} \quad [6]$$

16/3Here, c_1 and c_2 are system and implementation dependent coefficients, M is the total number of k-space samples, K_1 and K_2 are the convolution kernel widths in two spatial dimensions, and N is the total number of pixels of the convolved grid. While the exact computation time of the convolution depends on its implementation (36), it is evident that the convolution step is computationally expensive. Therefore, eliminating this operation from the iterative reconstruction leads to faster overall reconstruction time.

Data Acquisition

In this IRB-approved and HIPAA-compliant retrospective study, MR raw data from twenty-two male patients (age=64.78±6.67 years), who were referred for clinical DCE prostate MRI exam at our institute between 02/2017 and 06/2017 and who were imaged using a radial T_1-weighted GRE sequence, were collected. Written informed consent was waived.

Each patient dataset was acquired on a clinical 3T MR scanner (MAGNETOM Prisma, Siemens Healthineers, Germany) in transverse orientation using a fat-saturated 3D stack-of-stars golden-angle radial imaging sequence (1). Golden-angle radial sampling was employed in the k_x-k_y dimension, while Cartesian sampling was used along the slice dimension. Relevant imaging parameters were: TR/TE = 4.12/1.96 ms, matrix size = 224×224×(21–26), in-plane field of view (FOV) = 240×240 mm^2, voxel size = 1.07×1.07×3.0 mm^3, flip angle = 12°. 1755 spokes were acquired for each partition, resulting in an average total scan time of 197.45 ± 12.51 seconds. After ~15 seconds of the scan, a full-dose (0.1 mmol/kg of body weight) of contrast agent (Gadavist, Bayer Healthcare) was injected at a rate of 2 mL/sec.

Image Reconstruction

Both GRASP and GROG-GRASP reconstructions were performed in Matlab (Mathworks, MA). After coil-compression to 10 virtual channels (39), 26 consecutive spokes were

grouped for one dynamic frame, resulting in a temporal resolution of ~2-3 seconds/volume. The GROG reconstruction code was obtained from https://github.com/edibella/Reconstruction. First-order finite differences along the temporal dimension were chosen as the sparsifying transform T. To ensure a reasonable balance between image quality and temporal fidelity, a fixed regularization parameter was empirically selected, which was done separately for GRASP and GROG-GRASP (21). For GRASP, convolution gridding was performed with a 6×6 Kaiser-Bessel kernel and 1.5-fold oversampling. For GROG-GRASP, the weighting filter W (Eq. 5) was calculated with n=350 (≈224·π/2), which was empirically selected according to the Nyquist criterion. To assess the influence of the parameter n, the GROG-GRASP reconstruction was repeated with n=100 and n=1000 in one dataset.

The optimization problem for both reconstruction schemes was solved using a non-linear conjugate gradient algorithm. The stopping criterion for all reconstructions was set as 24 iterations or a change of the objective function smaller than 10^{-4}, whichever was achieved faster. Coil sensitivity maps were estimated from the static 3D image volume reconstructed from all spokes using the adaptive combination approach (40). To further improve processing speed, GROG-GRASP was additionally performed on GPUs by using the MATLAB function “gpuArray”. Following iFFT along the slice dimension, all slices of each dataset were reconstructed sequentially. Reconstructions were performed on a server equipped with 256 GB RAM and two 6-GB NVIDIA GPU cards. The reconstruction time for each dataset was recorded for comparison.

Image Analysis

The structural similarity index (SSIM) and root-mean-square error (RMSE) between GRASP and GROG-GRASP were calculated slice-by-slice for all datasets. The results were averaged over all slices and all subjects to represent mean ± standard deviation. Additionally, two regions of interest (ROIs) from a central slice of each dataset were manually drawn in the femoral artery and the prostate. The temporal signal profiles for these two ROIs were compared between GRASP and GROG-GRASP. First, the temporal signals were converted to relative enhancement signals as follows:

$$E(t) = \frac{S(t) - S_{baseline}}{S_{baseline}} \quad [8]$$

where S_{baseline} is the signal intensity before contrast enhancement, calculated by averaging the first five time points (~15s). The initial area under the curve (IAUC), which is calculated as the area under the curve for the first 90 seconds (41), was measured for all temporal signals:

$$IAUC(t) = \int_0^t E(\tau) d\tau \quad [9]$$

Additionally, the initial slope was determined:

$$Initial\ Slope = \frac{E(t_p)}{t_p} \quad [10]$$

where t_p is the time to a point where a given signal profile has the steepest gradient. IAUC and initial slope were averaged to represent mean ± standard deviation across all subjects, and Intraclass Correlation Coefficient (ICC) was calculated to assess the correlation between the signals computed from GRASP and GROG-GRASP.

Visual Image Quality Assessment

To assess image quality in a more clinically focused way, two post-contrast phases (one arterial phase and one delayed phase) were manually selected from each dataset. After pooling and randomizing the respective GRASP and GROG-GRASP images, two board-certified abdominal radiologists (H.C. and C.H., with 10 and 2 years of post-fellowship experience, respectively), who were blinded to the reconstruction schemes, scored overall image quality, sharpness of prostatic capsule and overall artifact level. A 4-point Likert-type scale was used for the scoring: overall image quality: 4=good, 3=adequate, 2=borderline, 1=non-diagnostic; sharpness of prostatic capsule: 4=good, 3=adequate, 2=partially seen, 1=not seen; overall artifact level: 4=none, 3=mild, 2=significant, 1= unreadable. The reported scores were averaged over the two readers and mean ± standard deviation was calculated for both contrast phases. A non-parametric paired two-tailed Wilcoxon signed-rank test was performed for statistical assessment, with a *P*-value less than 0.05 indicating statistical significance. Inter-reader variability was assessed using the Bland-Altman analysis.

Results

Figure 3 compares results from the GROG-GRASP reconstructions with different *W*. Reconstruction without additional weighting (W=1) generated noticeable blurring, which is consistent with the effect observed in Figure 1. Both image sharpness and convergence speed are improved when n increases. Similar results were obtained for n=350 and n=1000, confirming the selection of n=350 for GROG-GRASP.

Figure 4a compares GRASP with GROG-GRASP for three different temporal frames of a representative dataset. For all phases, no visual difference was observed between the two reconstruction schemes. Figure 4b shows the corresponding temporal signal profiles from two ROIs in the femoral artery and the prostate (red and yellow circles), suggesting high temporal correlation between the two methods.

The SSIM indexes and RMSE between GRASP and GROG-GRASP were 0.97 ± 0.01 and 0.007 ± 0.002, suggesting a high degree of similarity. The IAUC, initial slope, and ICC are summarized in Table 1a, indicating strong correlation between the temporal signal profiles generated from GRASP and GROG-GRASP. Table 1b summarizes the readers' scores. No significant difference (P>0.05) was found throughout all assessment categories. The inter-reader variability is shown in Figure S2 (supplementary materials). Reconstruction times for

GRASP and GROG-GRASP were 332.67 ± 32.83 minutes and 78.34 ± 8.04 minutes, respectively, averaged over all datasets. With GPU implementation, the reconstruction time of GROG-GRASP was further reduced to 14.04 ± 1.29 minutes (representative images are shown in supplementary Figure S3).

Discussion

In this work, we proposed a framework that combines GRASP with self-calibrating GROG. GROG-GRASP eliminates the requirement for the convolution gridding steps within the iterative optimization, thus enabling a substantial reduction of reconstruction time compared to conventional GRASP. The performance of GROG-GRASP was validated in a patient cohort, which is an important step prior to translation of this approach into clinical practice. The SSIM, RMSE, ICC, and visual image quality assessment suggested that the combination of GRASP with GROG preserves image quality and temporal fidelity. In addition, we have also optimized the reconstruction algorithm to further improve reconstruction performance by incorporating an additional filter during the iterative process. For the implementation of this filter, the parameter n has to be chosen. However, the exact choice of n only has a minor influence on image quality, and choosing n according to the Nyquist rate (n=base resolution·π/2) gave consistent results over all datasets used for this study.

Since GROG is used as a pre-processing step, it can benefit a broad range of iterative non-Cartesian reconstruction methods, including techniques based on k-space based or image-space based parallel imaging, compressed sensing, or their combinations. Prerequisites for successful implementation of GROG are a sufficient number of coil-array elements and adequate SNR (29). Given the wide-spread use of many-element coil arrays and the availability of a high-SNR dataset when all acquired radial spokes are combined for GROG calibration, these requirements are intrinsically fulfilled.

In this study, the performance of GROG-GRASP has been demonstrated for prostate imaging and therefore only for male subjects. However, the reconstruction performance of the proposed technique is independent of the particular application and can be extended to other applications such as cardiac or liver MRI.

Conclusion

GRASP reconstruction can be substantially accelerated using self-calibrating GROG as pre-processing step to obtain Cartesian k-space data. This permits elimination of the time-consuming gridding process from each iteration of the optimization process while maintaining image quality. The proposed combination shows promise towards implementation of GRASP and other iterative non-Cartesian reconstruction methods in clinical routine.

Supplementary Material

Refer to Web version on PubMed Central for supplementary material.

Acknowledgments

This work was supported in part by the NIH (P41 EB017183 and R01 EB018308) and was performed under the rubric of the Center for Advanced Imaging Innovation and Research (CAI^2R), an NIBIB Biomedical Technology Resource Center. The authors also thank Dr. Florian Knoll from the New York University School of Medicine, Dr. Tobias Wech from the University of Wuerzburg, and Dr. Daniel Staeb from the University of Queensland for helpful discussions.

References

1. Block KT, Chandarana H, Milla S, Bruno M, Mulholland T, Fatterpekar G, Hagiwara M, Grimm G, Geppert C, Kiefer B, Sodickson DK. Towards routine clinical use of radial stack-of-stars 3d gradient-echo sequences for reducing motion sensitivity. Journal of the Korean Society of Magnetic Resonance in Medicine. 18(2):87–106.
2. Aandal G, Nadig V, Yeh V, Rajiah P, Jenkins T, Sattar A, Griswold M, Gulani V, Gilkeson RC, Seiberlich N. Evaluation of left ventricular ejection fraction using through-time radial GRAPPA. J Cardiovasc Magn Reson. 2014; 16:79. [PubMed: 25315256]
3. Hulet JP, Greiser A, Mendes JK, McGann C, Treiman G, Parker DL. Highly accelerated cardiac cine phase-contrast MRI using an undersampled radial acquisition and temporally constrained reconstruction. Journal of magnetic resonance imaging : JMRI. 2014; 39(2):455–462. [PubMed: 23633229]
4. Jung H, Park J, Yoo J, Ye JC. Radial k-t FOCUSS for high-resolution cardiac cine MRI. Magnetic resonance in medicine. 2010; 63(1):68–78. [PubMed: 19859952]
5. Saybasili H, Herzka DA, Seiberlich N, Griswold MA. Real-time imaging with radial GRAPPA: Implementation on a heterogeneous architecture for low-latency reconstructions. Magnetic resonance imaging. 2014; 32(6):747–758. [PubMed: 24690453]
6. Liu J, Spincemaille P, Codella NC, Nguyen TD, Prince MR, Wang Y. Respiratory and cardiac self-gated free-breathing cardiac CINE imaging with multiecho 3D hybrid radial SSFP acquisition. Magnetic resonance in medicine. 2010; 63(5):1230–1237. [PubMed: 20432294]
7. Bauer RW, Radtke I, Block KT, Larson MC, Kerl JM, Hammerstingl R, Graf TG, Vogl TJ, Zhang S. True real-time cardiac MRI in free breathing without ECG synchronization using a novel sequence with radial k-space sampling and balanced SSFP contrast mode. Int J Cardiovasc Imaging. 2013; 29(5):1059–1067. [PubMed: 23334191]
8. Chandarana H, Block KT, Winfeld MJ, Lala SV, Mazori D, Giuffrida E, Babb JS, Milla SS. Free-breathing contrast-enhanced T1-weighted gradient-echo imaging with radial k-space sampling for paediatric abdominopelvic MRI. European radiology. 2014; 24(2):320–326. [PubMed: 24220754]
9. Chandarana H, Block TK, Rosenkrantz AB, Lim RP, Kim D, Mossa DJ, Babb JS, Kiefer B, Lee VS. Free-breathing radial 3D fat-suppressed T1-weighted gradient echo sequence: a viable alternative for contrast-enhanced liver imaging in patients unable to suspend respiration. Investigative radiology. 2011; 46(10):648–653. [PubMed: 21577119]
10. Chandarana H, Feng L, Block TK, Rosenkrantz AB, Lim RP, Babb JS, Sodickson DK, Otazo R. Free-breathing contrast-enhanced multiphase MRI of the liver using a combination of compressed sensing, parallel imaging, and golden-angle radial sampling. Investigative radiology. 2013; 48(1): 10–16. [PubMed: 23192165]
11. Benkert T, Feng L, Sodickson DK, Chandarana H, Block KT. Free-breathing volumetric fat/water separation by combining radial sampling, compressed sensing, and parallel imaging. Magnetic resonance in medicine. 2017; 78(2):565–576. [PubMed: 27612300]
12. Rosenkrantz AB, Geppert C, Grimm R, Block TK, Glielmi C, Feng L, Otazo R, Ream JM, Romolo MM, Taneja SS, Sodickson DK, Chandarana H. Dynamic contrast-enhanced MRI of the prostate with high spatiotemporal resolution using compressed sensing, parallel imaging, and continuous golden-angle radial sampling: preliminary experience. Journal of magnetic resonance imaging : JMRI. 2015; 41(5):1365–1373. [PubMed: 24833417]
13. Kim SG, Feng L, Grimm R, Freed M, Block KT, Sodickson DK, Moy L, Otazo R. Influence of temporal regularization and radial undersampling factor on compressed sensing reconstruction in

dynamic contrast enhanced MRI of the breast. Journal of magnetic resonance imaging : JMRI. 2016; 43(1):261–269. [PubMed: 26032976]

14. Chan RW, Ramsay EA, Cheung EY, Plewes DB. The influence of radial undersampling schemes on compressed sensing reconstruction in breast MRI. Magnetic resonance in medicine. 2012; 67(2):363–377. [PubMed: 21656558]
15. Benkert T, Block KT, Heller S, Moccaldi M, Sodickson DK, Kim SG, Moy L. Comprehensive Dynamic Contrast-Enhanced 3D Magnetic Resonance Imaging of the Breast With Fat/Water Separation and High Spatiotemporal Resolution Using Radial Sampling, Compressed Sensing, and Parallel Imaging. Investigative radiology. 2017
16. Rossi Espagnet MC, Bangiyev L, Haber M, Block KT, Babb J, Ruggiero V, Boada F, Gonen O, Fatterpekar GM. High-Resolution DCE-MRI of the Pituitary Gland Using Radial k-Space Acquisition with Compressed Sensing Reconstruction. AJNR Am J Neuroradiol. 2015; 36(8): 1444–1449. [PubMed: 25953760]
17. Bangiyev L, Raz E, Block TK, Hagiwara M, Wu X, Yu E, Fatterpekar GM. Evaluation of the orbit using contrast-enhanced radial 3D fat-suppressed T1 weighted gradient echo (Radial-VIBE) sequence. The British journal of radiology. 2015; 88(1054):20140863. [PubMed: 26194589]
18. Zhou Z, Han F, Yu S, Yu D, Rapacchi S, Song HK, Wang DJJ, Hu P, Yan L. Accelerated noncontrast-enhanced 4-dimensional intracranial MR angiography using golden-angle stack-of-stars trajectory and compressed sensing with magnitude subtraction. Magnetic resonance in medicine. 2017
19. Block KT, Uecker M, Frahm J. Undersampled radial MRI with multiple coils. Iterative image reconstruction using a total variation constraint Magnetic resonance in medicine. 2007; 57(6): 1086–1098. [PubMed: 17534903]
20. Adluru G, McGann C, Speier P, Kholmovski EG, Shaaban A, Dibella EV. Acquisition and reconstruction of undersampled radial data for myocardial perfusion magnetic resonance imaging. Journal of magnetic resonance imaging : JMRI. 2009; 29(2):466–473. [PubMed: 19161204]
21. Feng L, Grimm R, Block KT, Chandarana H, Kim S, Xu J, Axel L, Sodickson DK, Otazo R. Golden-angle radial sparse parallel MRI: combination of compressed sensing, parallel imaging, and golden-angle radial sampling for fast and flexible dynamic volumetric MRI. Magnetic resonance in medicine. 2014; 72(3):707–717. [PubMed: 24142845]
22. Feng L, Benkert T, Block KT, Sodickson DK, Otazo R, Chandarana H. Compressed sensing for body MRI. Journal of magnetic resonance imaging : JMRI. 2017; 45(4):966–987. [PubMed: 27981664]
23. Glover GH, Pauly JM. Projection reconstruction techniques for reduction of motion effects in MRI. Magnetic resonance in medicine. 1992; 28(2):275–289. [PubMed: 1461126]
24. Winkelmann S, Schaeffter T, Koehler T, Eggers H, Doessel O. An optimal radial profile order based on the Golden Ratio for time-resolved MRI. IEEE transactions on medical imaging. 2007; 26(1):68–76. [PubMed: 17243585]
25. Block KT, Feng L, Grimm R, Chandarana H, Otazo R, Geppert C, Sodickson DK. GRASP: Tackling the challenges of abdominopelvic DCE-MRI. Magnetom Flash. 2014; 5:16–22.
26. Wajer, FTAW., Pruessmann, KP. Major speedup of reconstruction for sensitivity encoding with arbitrary trajectory; Proceedings of the 9th Annual Meeting of ISMRM; Glasgow, Scotland, UK. 2001. p. 767
27. Fessler JA, Lee S, Olafsson VT, Shi HR, Noll DC. Toeplitz-based iterative image reconstruction for MRI with correction for magnetic field inhomogeneity. Ieee T Signal Proces. 2005; 53(9):3393–3402.
28. Uecker M, Zhang S, Frahm J. Nonlinear inverse reconstruction for real-time MRI of the human heart using undersampled radial FLASH. Magnetic resonance in medicine. 2010; 63(6):1456–1462. [PubMed: 20512847]
29. Seiberlich N, Breuer FA, Blaimer M, Barkauskas K, Jakob PM, Griswold MA. Non-Cartesian data reconstruction using GRAPPA operator gridding (GROG). Magnetic resonance in medicine. 2007; 58(6):1257–1265. [PubMed: 17969027]

30. Tran-Gia J, Stab D, Wech T, Hahn D, Kostler H. Model-based Acceleration of Parameter mapping (MAP) for saturation prepared radially acquired data. Magnetic resonance in medicine. 2013; 70(6):1524–1534. [PubMed: 23315831]

31. Wech T, Seiberlich N, Schindele A, Grau V, Diffley L, Gyngell ML, Borzi A, Kostler H, Schneider JE. Development of Real-Time Magnetic Resonance Imaging of Mouse Hearts at 9.4 Tesla–Simulations and First Application. IEEE transactions on medical imaging. 2016; 35(3):912–920. [PubMed: 26595913]

32. Shahzadi, I., Aslam, I., Qazi, SA., Omer, H. GRAPPA operator gridding (GROG) for optimized L + S GRASP reconstruction of dynamic contrast enhanced MRI; Proceedings of 2016 Annual Meeting of ESMRMB; Vienna, Austria. p. 122

33. Shahzadi, I., Aslam, I., Qazi, SA., Omer, H. Optimized GRASP for dynamic contrast enhanced MRI using GRAPPA operator gridding (GROG) and iterative soft-thresholding; Proceedings of 2016 Annual Meeting of ESMRMB; Vienna, Austria. p. 126

34. Tian Y, Erb KC, Adluru G, Likhite D, Pedgaonkar A, Blatt M, Kamesh Iyer S, Roberts J, DiBella E. Evaluation of Pre-reconstruction Interpolation Methods for Iterative Reconstruction of Radial k-Space Data. Med Phys. 2017 Aug; 44(8):4025–4034. 2017. [PubMed: 28543266]

35. Seiberlich N, Breuer F, Blaimer M, Jakob P, Griswold M. Self-calibrating GRAPPA operator gridding for radial and spiral trajectories. Magnetic resonance in medicine. 2008; 59(4):930–935. [PubMed: 18383296]

36. Fessler JA, Sutton BP. Nonuniform fast Fourier transforms using min-max interpolation. Ieee T Signal Proces. 2003; 51(2):560–574.

37. Mailhe, B., Wang, Q., Grimm, R., Nickel, MD., Block, KT., Chandarana, H., Nadar, MS. Density compensation for iterative reconstruction from under-sampled radial data; Proceedings of the 23rd Annual Meeting of ISMRM; Toronto, Canada. 2015. p. 2452

38. Ou T. gNUFFTW. Auto-Tuning for High-Performance GPU-Accelerated Non-Uniform Fast Fourier Transforms. EECS Department, University of California; Berkeley: May 12. 2017 Technical Report No. UCB/EECS-2017-90http://www2.eecs.berkeley.edu/Pubs/TechRpts/2017/EECS-2017-90.pdf

39. Huang F, Vijayakumar S, Li Y, Hertel S, Duensing GR. A software channel compression technique for faster reconstruction with many channels. Magnetic resonance imaging. 2008; 26(1):133–141. [PubMed: 17573223]

40. Walsh DO, Gmitro AF, Marcellin MW. Adaptive reconstruction of phased array MR imagery. Magnetic resonance in medicine. 2000; 43(5):682–690. [PubMed: 10800033]

41. Cuenod CA, Balvay D. Perfusion and vascular permeability: basic concepts and measurement in DCE-CT and DCE-MRI. Diagn Interv Imaging. 2013; 94(12):1187–1204. [PubMed: 24211260]

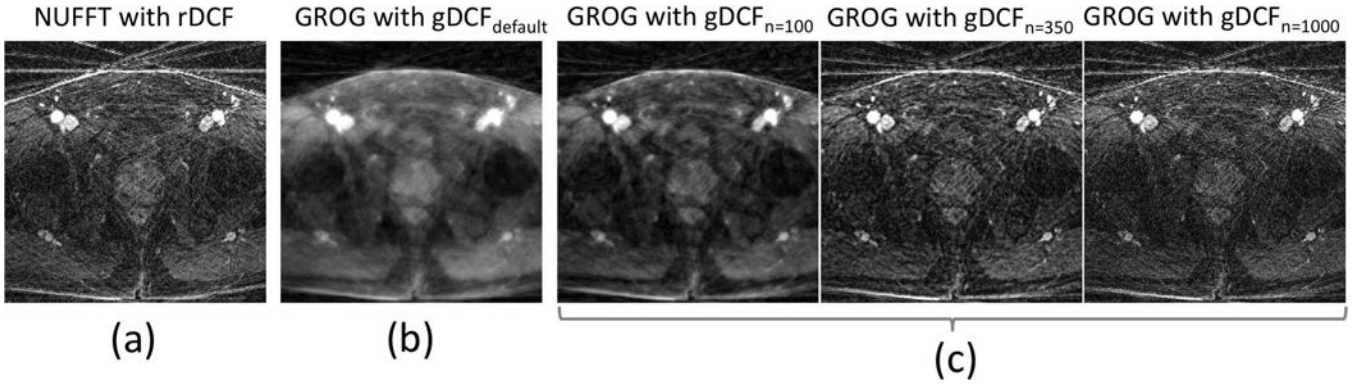

Figure 1.

Comparison between NUFFT-based and GROG-based reconstruction of an undersampled dataset with 26 radial projections. While the reconstruction with NUFFT leads to a sharp image with dominant streaking artifacts (a), a standard GROG implementation with $gDCF_{default}$ inherently prefers SNR over resolution, which introduces blurring (b). This can be overcome by modifying the GROG density compensation function ($gDCF_n$ (c)), where n denotes the number of spokes which is used for the design of this filter. With increasing n, the blurring is resolved and results are similar compared to the image obtained with NUFFT.

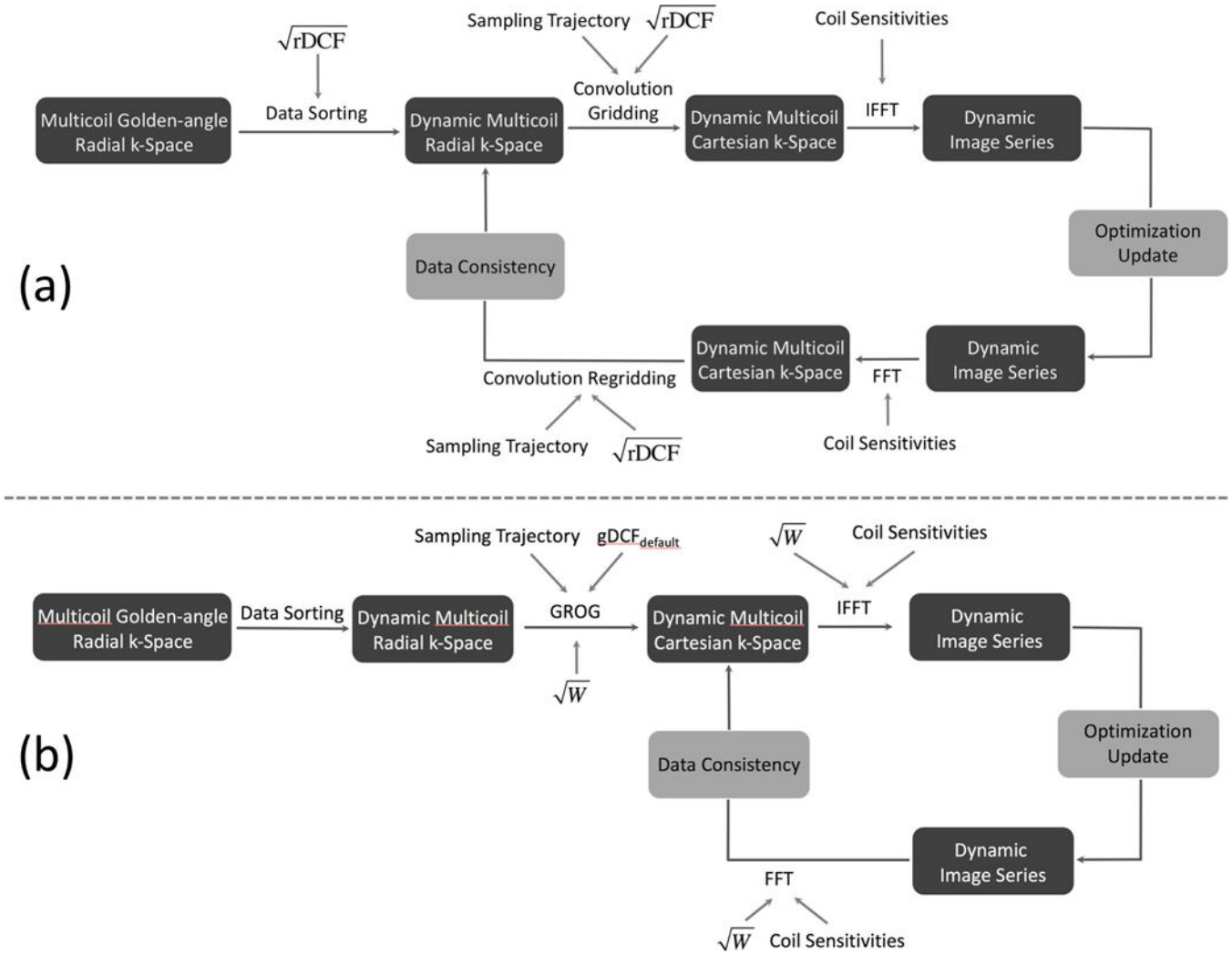

Figure 2.

Reconstruction pipeline of conventional GRASP (a) and GROG-GRASP (b). For GRASP, computationally expensive convolution gridding and regridding steps are performed in each iteration. For GROG-GRASP, this is overcome by shifting the acquired radial k-space data with GROG on a conventional Cartesian grid as pre-processing step. Similar to the radial DCF (rDCF) which is repeatedly applied during the conventional GRASP reconstruction, a weighting filter W is employed for GROG-GRASP to improve reconstruction performance.

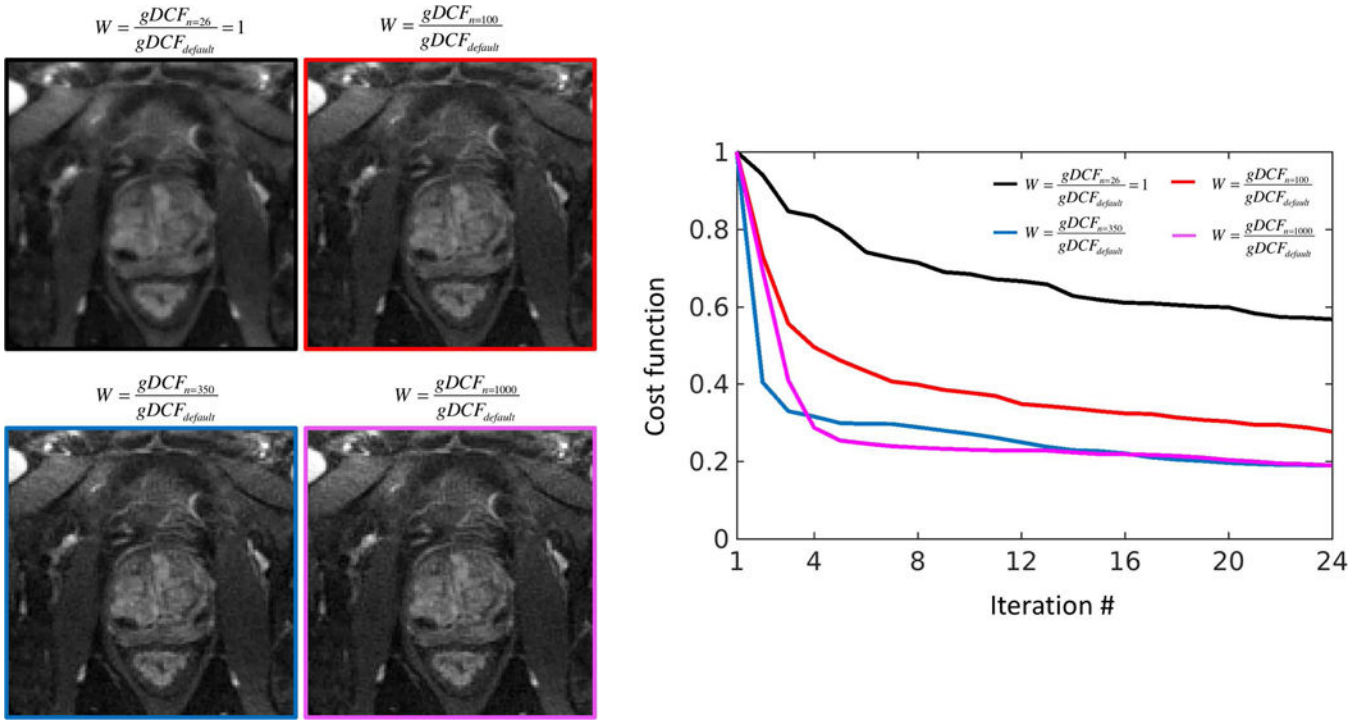

Figure 3.

Influence of the design of the weighting filter W on GROG-GRASP image quality. Reconstruction without an additional filter (n=26, W=1) leads to slow convergence and blurring, which is improved when an additional filter (n>26) is used. While slight blurring remains for n=100, sharp images and rapid convergence are achieved when choosing n according to the Nyquist criterion (n=base resolution·π/2≈350). Results are similar when using higher n (e.g., n=1000), suggesting that image quality is consistent within a certain range for n.

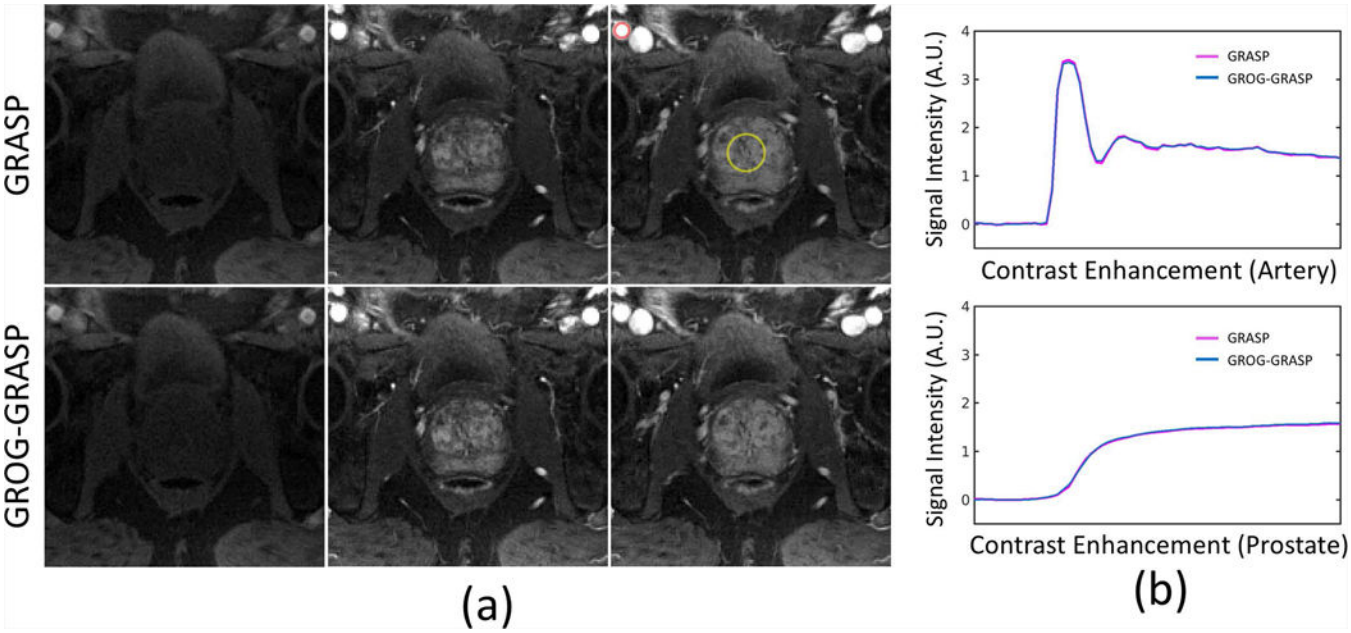

Figure 4.

(a) Three different contrast phases, reconstructed with standard GRASP (first row) and GROG-GRASP (second row). No visual differences can be seen between the two methods. This finding is confirmed by the temporal signal profiles, which show high temporal correlation (b).

Table 1(a)

Summary of the IAUC (initial area under the curve) and the initial slope of the temporal signals, which were computed in the femoral artery and in the prostate. The ICC (intraclass correlation coefficient) indicates that the temporal signals are well-correlated between GRASP and GROG-GRASP.

		IAUC	ICC (IAUC)	Initial Slope	ICC(Initial Slope)
Femoral Artery	GRASP	72.38±17.78	0.999	0.021±0.01	0.948
	GROG-GRASP	71.49±17.93		0.022±0.01	
Prostate	GRASP	51.92±18.17	0.999	0.01±0.00	0.980
	GROG-GRASP	52.42±17.92		0.01±0.00	

Table 1(b)

Qualitative comparison between GRASP and GROG-GRASP for two contrast-enhancement phases. No significant differences (P>0.05) between the two reconstruction schemes were found in all assessed categories.

		Overall Image Quality	Sharpness of Prostatic Capsule	Overall Artifact Level
Arterial Phase	GRASP	3.07±0.48	3.07±0.51	3.00±0.47
	GROG-GRASP	3.05±0.47	3.10±0.52	3.02±0.51
Delayed Phase	GRASP	3.55±0.38	3.73±0.34	3.52±0.40
	GROG-GRASP	3.52±0.40	3.69±0.40	3.50±0.42

Scoring criteria:

For overall image quality, 4=good, 3=adequate, 2=borderline, 1=non-diagnostic.

For sharpness of prostatic capsule, 4=good, 3=adequate, 2=partially seen, 1=not seen.

For overall artifacts level: 4=none, 3=mild, 2=significant, 1=unreadable